© 2016. Published by The Company of Biologists Ltd | Journal of Cell Science (2016) 129, 3342-3350 doi:10.1242/jcs.187112

RESEARCH ARTICLE

Trafficking of MHC molecules to the cell surface creates dynamic protein patches

Daniel Blumenthal[1,*], Michael Edidin[2] and Levi A. Gheber[1,‡]

ABSTRACT

Major histocompatibility complex class I (MHC-I) molecules signal infection or transformation by engaging receptors on T lymphocytes. The spatial organization of MHC-I on the plasma membranes is important for this engagement. We and others have shown that MHC-I molecules, like other membrane proteins, are not uniformly distributed, but occur in patches in the plasma membrane. Here, we describe the temporal details of MHC-I patch formation and combine them with the spatial details, which we have described earlier, to yield a comprehensive quantitative description of patch formation. MHC-I is delivered to the plasma membrane in clathrin-coated vesicles, arriving at a rate of $\sim 2.5\times10^{-3}$ μm^{-1} min^{-1} (or about two arrivals per minute over the whole cell). The vesicles dock and fuse at non-random, apparently targeted, locations on the membrane and the newly delivered MHC-I molecules form patches that are a few hundred nanometers in diameter. The patches are maintained at steady state by a dynamic equilibrium between the rate of delivery and the rate of hindered diffusion of MHC-I molecules out of the patches (caused by components of the actin cytoskeleton).

KEY WORDS: Major histocompatibility complex class I, MHC-I, Total internal reflection fluorescence microscopy, TIRFM, Fluorescence recovery after photobleaching, FRAP, Obstructed diffusion, Membrane trafficking

INTRODUCTION

Plasma membrane lipids and proteins are enriched within areas of the plasma membrane to form patches of different sizes (Vereb et al., 2003; Engelman, 2005). There are likely different mechanisms for patch formation on a variety of scales. Nanometer-scale patches have been variously proposed to arise due to differences in interaction energies among membrane proteins (Engelman, 2005) or to coupling of membrane lipids to the actin-based membrane cytoskeleton (Gowrishankar et al., 2012). At scales of 100s of nm, patches might be stabilized by constraints on lateral diffusion of their component molecules. Some of these constraints arise from physical barriers created by the actin mesh of the membrane skeleton (Sako and Kusumi, 1995), or by anchoring of membrane proteins to that skeleton (Feder et al., 1996).

[1]The Avram and Stella Goldstein-Goren Department of Biotechnology Engineering, Ben Gurion University of the Negev, Beer-Sheva, 8410501 Israel. [2]Department of Biology, Johns Hopkins University, Baltimore, MD 21218, USA.
*Present addresses: Department of Pathology and Laboratory Medicine, Children's Hospital of Philadelphia Research Institute, Philadelphia, PA, USA and Department of Pathology and Laboratory Medicine, University of Pennsylvania Perelman School of Medicine, Philadelphia, PA, USA

‡Author for correspondence (glevi@bgu.ac.il)

D.B., 0000-0002-9207-5848; L.A.G., 0000-0002-7909-100X

Received 4 February 2016; Accepted 21 July 2016

In a series of studies, we have explored the propensity of major histocompatibility complex class I (MHC-I) molecules to form patches. These type I transmembrane glycoproteins are expressed on virtually all mammalian cells and are a useful model for membrane proteins generally. Patches of MHC-I and MHC-II molecules are also specifically important in activating T-cell responses to antigen-presenting cells (Fooksman et al., 2006; Turley et al., 2000). We used super-resolution near-field scanning optical microscopy (NSOM) (Hwang et al., 1998) as well as a deconvolution approach on conventional images (Tang and Edidin, 2001) to directly image immunostained MHC-I on the membrane, and found these patches to be 300–700 nm in diameter. We also estimated the number of molecules in a single patch to be 25–250, in good agreement with previous results (Hwang et al., 1998; Tang and Edidin, 2001).

MHC-I molecules diffuse in the plane of the plasma membrane, as measured by fluorescence recovery after photobleaching (FRAP) and by single-particle tracking (SPT) (Yechiel and Edidin, 1987; Edidin et al., 1994; Kusumi and Sako, 1996). Hence, the persistence of patches containing hundreds of molecules was unexpected. To explain these patches, we proposed a quantitative dynamic model in which patches arise upon delivery of a bolus of newly synthesized MHC-I molecules by fusion of an exocytic vesicle with the cell surface, and disperse by lateral diffusion, hindered by the actin mesh of the membrane (Gheber and Edidin, 1999). Our model does not require lateral interactions between MHC-I molecules in a patch. Rather, the arrival of vesicles containing newly synthesized MHC-I to the membrane creates a high concentration at the site of vesicle fusion; this high concentration of MHC-I gradually decays by lateral diffusion of molecules hindered by dynamic barriers, while new vesicle arrivals maintain the distribution of MHC-I in patches at steady state. Computer simulations based on the model predicted that should barriers to diffusion be removed or vesicle trafficking hindered, membrane patches would decay towards a uniform distribution of MHC-I molecules on the cell membrane. Scaling the simulations to biological dimensions (based on literature values for vesicle trafficking, frequency of actin barriers opening and lateral diffusion), the lifetime of a single patch of MHC-I was predicted to be ~20 s.

In order to validate our model, we directly measured patch lifetime by total internal reflection fluorescence microscopy (TIRFM) imaging of MHC-I–GFP, reporting a mean patch lifetime of ~40 s in good agreement with the model prediction (Lavi et al., 2007). In these measurements, formation and dispersion of patches was seen as a sharp increase in fluorescence intensity (as a result of an exocytic vesicle fusion event) followed by an exponential decay (describing the dispersion of labeled molecules by diffusion across dynamic barriers). Observations of consecutive delivery events in the same position on the cell membrane pointed to the possibility that delivery might occur at specific, nonrandom sites on the membrane; such a scenario favors patching over the random

Journal of Cell Science

Journal of Cell Science (2016) 129, 3342-3350 doi:10.1242/jcs.187112

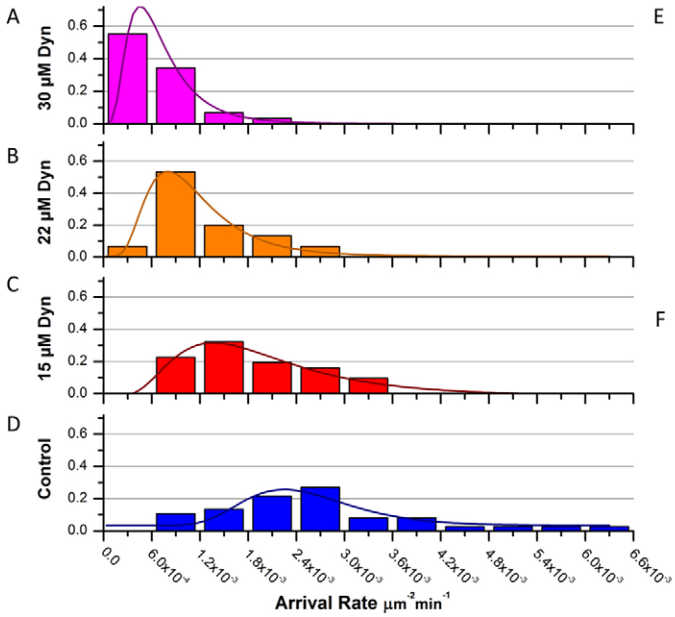

E

Cell Group	Mean Arrival Rate $[\mu m^{-2} min^{-1}]$	Mode Arrival Rate $[\mu m^{-2} min^{-1}]$
Control	2.67×10^{-3}	2.70×10^{-3}
15 μM Dynasore	1.86×10^{-3}	1.50×10^{-3}
22 μM Dynasore	1.26×10^{-3}	0.90×10^{-3}
30 μM Dynasore	0.68×10^{-3}	0.30×10^{-3}

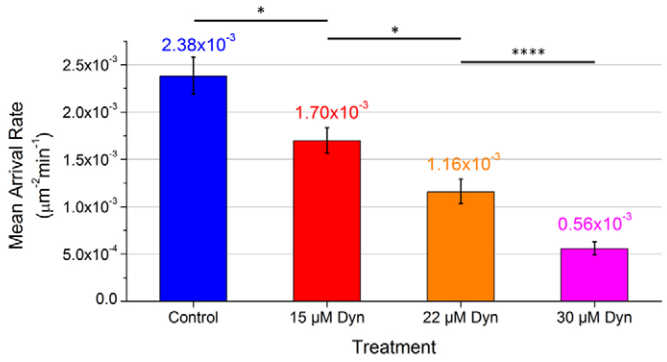

Fig. 1. Distributions of vesicle arrival rates for control and Dynasore-treated cells. Distributions are positively skewed; lines represent fits to log-normal distributions, and serve as a guide to the eye. (A) Distribution of arrival rates of cells treated with 30 μM Dynasore (Dyn) (*n*=29). (B) Distribution of arrival rates of cells treated with 22 μM Dynasore (*n*=15). (C) Distribution of arrival rates of cells treated with 15 μM Dynasore (*n*=31). (D) Distribution of arrival rates of control (untreated) cells (*n*=37). (E) Means and modes of vesicle arrival rates for the four treatment groups. (F) Means of log transformed distributions (shown in E) are significantly different from each other. Error bars represent s.e.m. **P*<0.05, *****P*<0.0001 (one-way ANOVA, Holm-Sidak all-pairwise test).

location assumption of our model. We demonstrated the role of the actin cytoskeleton in maintaining MHC-I patches by treating the cells with actin-modulating toxins (Lavi et al., 2012). Stabilization and destabilization of actin filaments resulted in increased and decreased MHC-I patch lifetimes, respectively.

Supporting evidence for the importance of vesicle trafficking came from an experiment in which clathrin-mediated vesicle traffic was reduced by introducing a dominant-negative dynamin (a GTPase important for clathrin-mediated endocytosis) into cells (Tang and Edidin, 2001). The logic here was that cells in culture generally maintain a constant surface area at steady state, therefore internalization of membrane by endocytosis is compensated for by increased exocytosis (Houy et al., 2013; Patzak and Winkler, 1986; Smith and Neher, 1997). This is also seen at neuronal synapses (Haucke et al., 2011). Hence, inhibiting endocytosis was expected to decrease the rate of exocytosis of MHC-I molecules. Although the methods used previously only partially blocked vesicle traffic, they resulted in more diffuse patches, which could be attributable to MHC-I molecule diffusion away from a site of vesicle fusion in the absence of further delivery of more MHC-I to the cell surface. Although providing supporting evidence for the predicted importance of vesicle traffic in maintaining MHC-I patches at steady state, those measurements were performed on immunostained, fixed cells. In order to directly link the vesicle arrival rate and apparent size of patches, here, we use GFP-tagged MHC-I molecules and live imaging [in total internal reflection fluorescence microscopy (TIRFM), to exclude fluorescence from the cell cytoplasm], in order to count the number of delivery events in real time. After quantifying the arrival rate of vesicles trafficking MHC-I to the membrane in normal cells, we then reduce it by treating cells with increasing doses of the dynamin inhibitor Dynasore (Macia et al., 2006). Using Dynasore or a dominant-negative dynamin mutant (as in Tang and Edidin, 2001) has the same logic – slowing of the trafficking rate. However, using Dynasore in combination with live imaging and counting of delivery events allows us to unequivocally establish a dose-dependent control of the MHC-I delivery rate to the plasma membrane. Using this delivery-rate modulation approach, we further demonstrate that the reduction of delivery rate results in a proportional dispersion of patches.

Direct measurements of both the arrival rate of vesicles trafficking MHC-I and patch size demonstrates for the first time the existence of an inverse correlation between these two parameters. It demonstrates the prediction of the simulation-assisted model, according to which barriers to lateral diffusion alone are not sufficient to maintain MHC-I patches at steady state. A continuous delivery of new MHC-I molecules to the plasma membrane, at a specific rate, is essential. The size of observed patches at steady state is thus determined by a combination of delivery rate and escape rate over barriers to lateral diffusion. We also present evidence that, as is found in neuronal cells (Robinson et al., 1995), vesicles fuse with the surface membrane at specific hotspots.

RESULTS

Quantification of vesicle arrival at the plasma membrane

To quantify the arrival rate of vesicles trafficking MHC-I to the plasma membrane, a series of time-lapse images (a stack) was acquired, with equal exposure time per frame and a total sampling time of 8–12 min. Exposure time varied between 2 to 3 s per frame depending on the brightness of the cells under investigation; the time interval between consecutive frames was usually 1 s. To decrease the vesicle arrival rate, we used Dynasore, a potent inhibitor of dynamin-dependent endocytic pathways (clathrin-coated vesicles) (Macia et al., 2006) recently shown to also affect exocytosis (Jaiswal et al., 2009; Anantharam et al., 2011, 2012). Dynasore concentrations of 15 μM, 22 μM and 30 μM were used. The lowest concentration has been reported as the median inhibitory

Journal of Cell Science (2016) 129, 3342-3350 doi:10.1242/jcs.187112

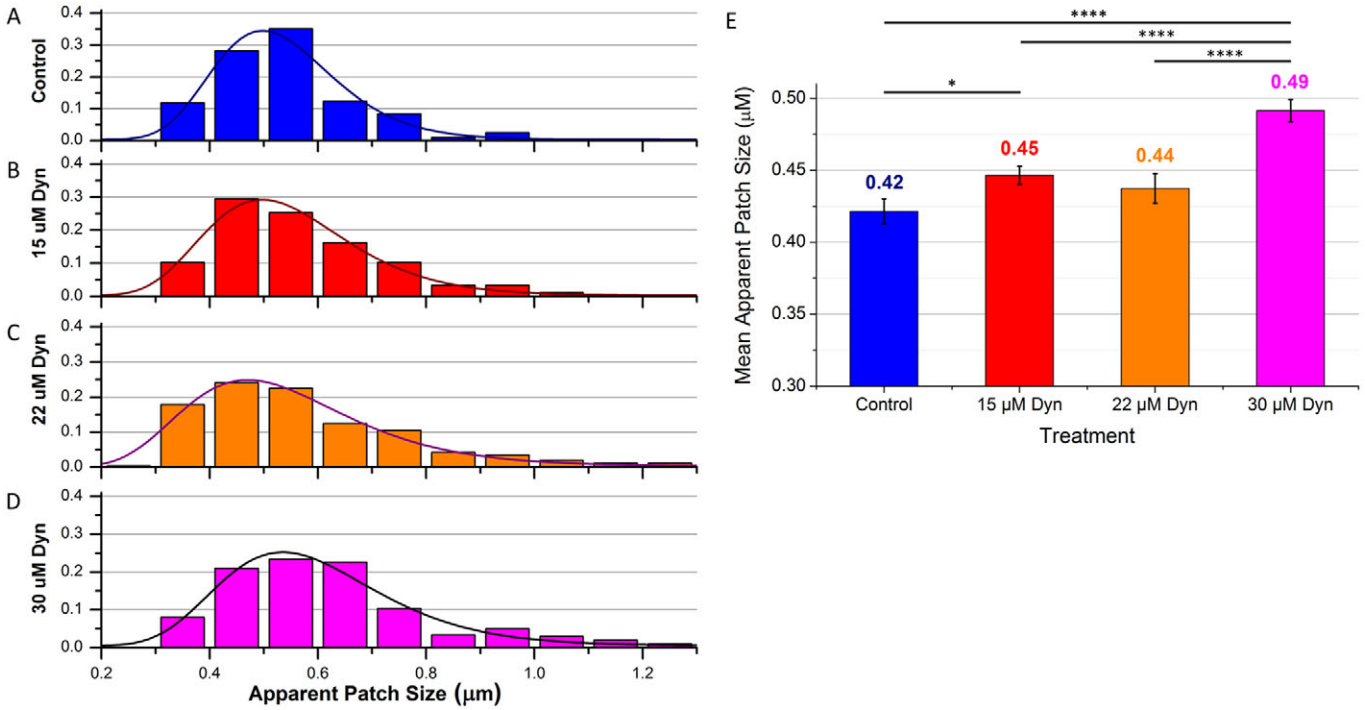

Fig. 2. Distributions of patch sizes for control and Dynasore-treated cells. (A–D) Each cell image was cropped into multiple smaller images, to exclude background, then each crop was spatially (2D) auto-correlated to extract the size of a typical patch in that crop (see Materials and Methods for details). The distributions of these typical patch sizes in each crop are presented in A–D for the indicated Dyansore (Dyn) concentration. Cell and crop numbers as follows: A, control (untreated) cells, *n*=37 cells, *n*=202 crops; B, 15 µM Dynasore, *n*=31 cells, *n* =508 crops; C, 22 µM Dynasore, *n*=15 cells, *n* =257 crops; D, 30 µM Dynasore, *n*=29 cells, *n*=500 crops. The peaks of the distributions are visibly shifted to the right (mean patch size increases) as Dynasore concentration increases. (E) Means of log transformed distributions are significantly different from each other. Error bars represent s.e.m. **P*<0.05, *****P*<0.0001 (one-way ANOVA, Holm-Sidak all-pairwise test).

concentration (IC_{50}) of 15 µM (Macia et al., 2006); the highest is less than the concentration, 40 µM, known to disrupt cell functions, for instance by destabilizing F-actin (Yamada et al., 2009). We analyzed the four different treatment groups (see Materials and Methods, arrival rate analysis) and produced distributions of arrival rates for each group (Fig. 1A–D). All four distributions were positively skewed; the means and modes of the distributions are given in Fig. 1F. From these distributions the mean vesicle arrival rate was calculated as 2.67×10^{-3} arrivals/µm^2 min with an average sampled cell area of ~700 µm^2, or ~2.0 arrivals per cell every minute. The skewed distributions were log transformed to obtain approximately normal distributions (Fig. S1A). The means of the transformed data for the four treatment groups were compared and found to be significantly different from each other (one-way ANOVA, followed by Holm-Sidak multiple comparison test, $P<0.0001$, Fig. 1E).

Assessment of patch size

To measure patch size, we used an image (2D) autocorrelation approach, as described in the Materials and Methods. The distribution of patch sizes for each of the four treatment groups is presented in Fig. 2A–D. The mean patch size in cells treated with 30 µM Dynasore is significantly larger than that of all other groups ($P<0.0001$); the mean patch size in cells treated with 15 µM Dynasore group is significantly larger than that of the untreated cells ($P<0.05$) (one-way ANOVA followed by Holm-Sidak multiple comparison test, Fig. 2E). The difference between the observed mean patch sizes of cells treated with 15 µM Dynasore and cells treated with 22 µM Dynasore is not statistically significant, consistent with the fact that patch sizes approach the diffraction limit of our system, so that small changes cannot be resolved. However, the trend of increased patch size with increased Dynasore concentration is evident.

Sites of MHC-I delivery

In order to determine whether delivery of MHC-I to the surface occurs at random positions, or specific 'hotspots', we photobleached a large area of a cell, 'erasing' the MHC-I present on the plasma membrane, and followed the appearance of patches of newly delivered GFP–MHC-I. About one-third of an imaged cell was photobleached, and fluorescence recovery was monitored for a total of 20 min, at 20-s intervals (Fig. 3A). In the recovered image (representing the maximal recovery after bleaching), it is easy to observe that the MHC-I is still distributed in patches. To qualitatively assess whether the newly formed patches are located at the same positions as the old (photobleached) ones, we aligned the image of the cell after full recovery ('recovered' image) to the image of the cell prior to photobleaching ('prebleach' image). Alignment was achieved by implementing a cross-correlation procedure yielding the relative displacement between the two images (see Materials and Methods). Then, the 'prebleach' image was pseudo-colored red, and the 'recovered' image was pseudo-colored green (Fig. 3B,C).

The two images were then superimposed, creating a colocalization image (Fig. 3D). The overlaid image shows red, green and yellow areas corresponding to non-recovered (existed before but do not exist after photobleaching), newly formed (did not exist before but do exist after photobleaching) and recovered patches

Journal of Cell Science (2016) 129, 3342-3350 doi:10.1242/jcs.187112

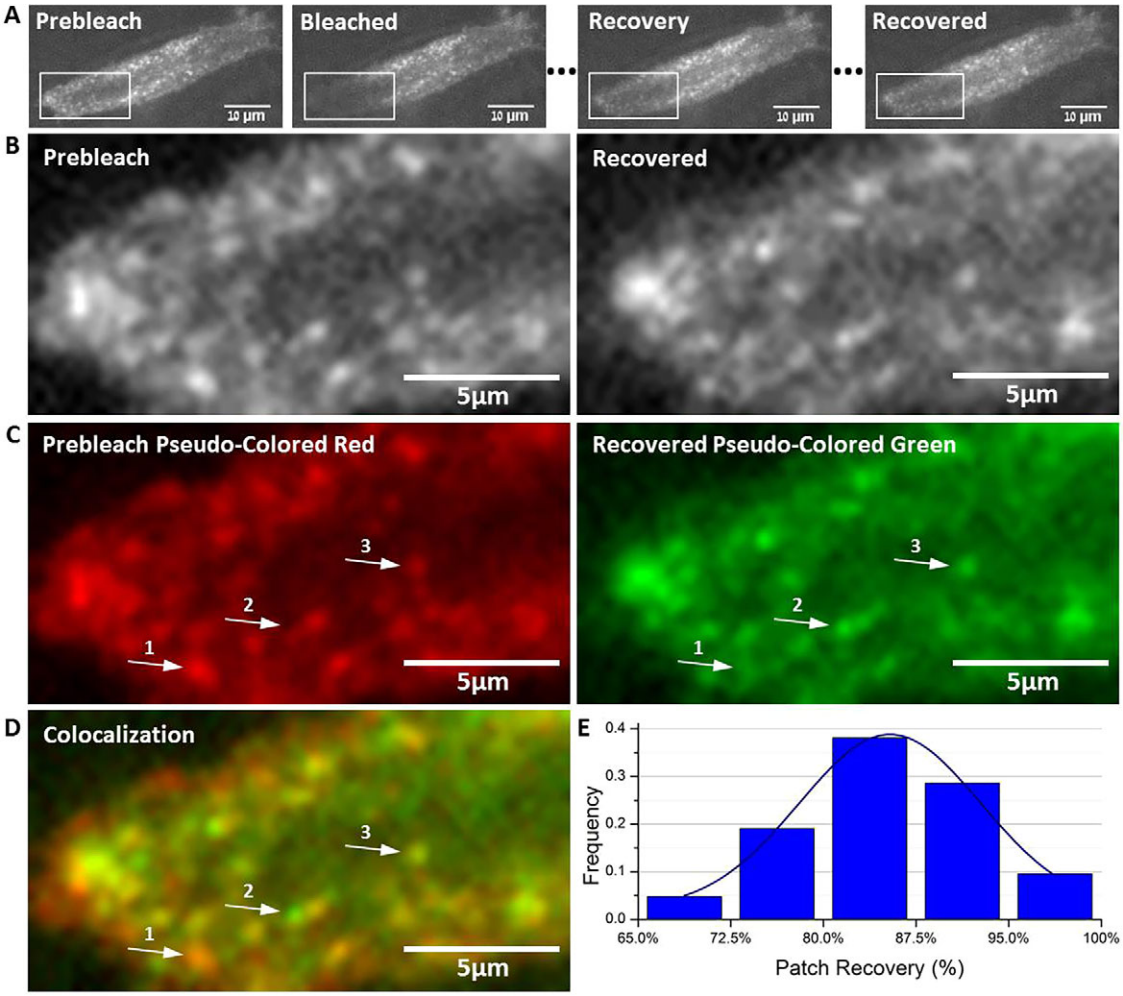

Fig. 3. Patch location and recovery analysis. (A) Part of a recovery stack. (B) Crop of the bleached area only in the 'prebleach' and 'recovered' images. The recovered image was scaled to the dynamic range of the prebleach image. (C) The prebleach image was pseudo-colored red and the recovered image pseudo-colored green. (D) The colocalization image shows red (for example, arrow 1), green (for example, arrow 2) and yellow (for example, arrow 3) areas corresponding to non-recovered, newly formed and recovered patches. (E) The recovery fraction is normally distributed with a mean±s.d. of 85.2±7.7% (n=21).

(existed before and exist after photobleaching). To quantitatively describe the extent of recovery, the number of recovered patches in the recovered image that colocalize with a mask obtained from the prebleach image was counted. Having analyzed 21 different series in such a way, we obtained a distribution of the 'percentage recovery' of patch positions. Fitting a normal distribution to our data, we obtain a mean recovery fraction of 85.2±7.7% (mean±s.d.) (Fig. 3E). These results strongly indicate that the majority of MHC-I-containing vesicles are targeted to specific, non-random locations on the plasma membrane.

Assessing the diffusion coefficient for GFP-tagged H-2L^d molecules by recovery simulations

We used our recently developed FRAP analysis method, 'simFRAP' (Blumenthal et al., 2015), to extract the diffusion coefficient of tagged MHC-I molecules on the cell membrane using the same 21 series acquired for the analysis described in the above section. The resulting mean±s.d. diffusion coefficient was $1.13\pm0.1\times10^{-9}$ cm^2/s, in good agreement with obstructed diffusion regime (D_{Macro}) of MHC-I molecules in the plasma membrane (Edidin, 1987). The simFRAP algorithm receives a multiple-frame TIFF file, representing the experiment as input and simulates the (pure) diffusion of the fluorescent probes (2D random walk) starting with the first post-bleach frame of the actual data as its implicit boundary and initial conditions. Comparing the real recovery data (Fig. 4, closed circles) with simulated data (Fig. 4, blue dots) it is clear that the first ∼9 min of recovery are very well described by pure lateral diffusion (of unbleached molecules from the approximate two-thirds of the cell that was unbleached, into the approximate one-third of the cell that was bleached). The experimental data after ∼9 min (9.1±2.3 min, n=9) show higher recovery of fluorescence than predicted by pure diffusion.

DISCUSSION

The mechanism behind the formation and persistence of dynamic MHC-I patches allows control over immune-presentation to T-cells. Although past work has unraveled major parts of the mechanism behind patching, allowing the formation of a model explaining the creation and persistence of MHC-I patches in steady-state, several parameters of the model were not examined experimentally. Here, we have measured these parameters and further expanded our model.

As predicted by our model, the trafficking of MHC-I to the membrane via vesicles is crucial for the dynamics of MHC-I patch

Journal of Cell Science (2016) 129, 3342-3350 doi:10.1242/jcs.187112

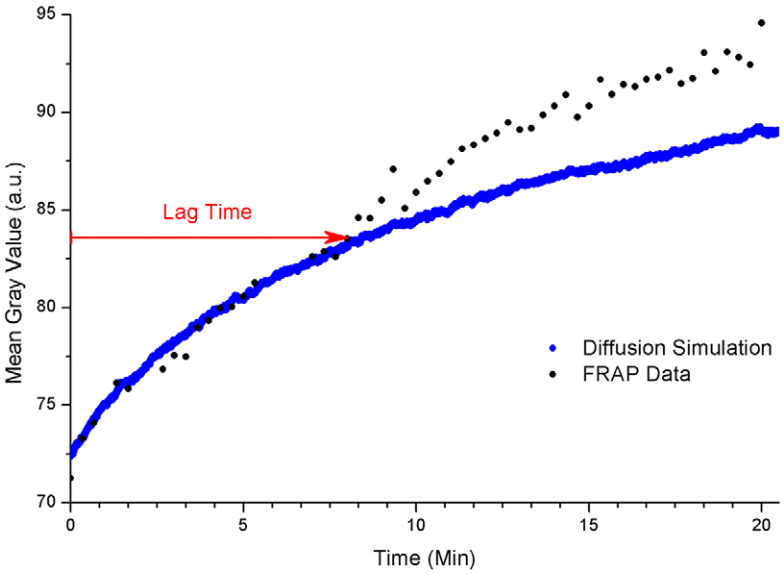

Fig. 4. Typical comparison between simulated and real FRAP data. A fitting of the 2D diffusion simulation to experimental FRAP data. The first part of recovery is in excellent agreement with the simulation of pure lateral diffusion. After a lag time (red arrow), recovery diverges from the simulation and the two data sets reach a different final value, pointing to the arrival of new fluorescent material to the membrane.

formation. Vesicle arrival events were quantified and found to be ~2 arrivals per cell every min. Previously reported data suggests an expected vesicle arrival rate of ~30 arrivals per cell every min for all exocytic vesicles (Jaiswal et al., 2009). Comparison of the two values suggests that a substantial fraction of exocytic vesicles are trafficking MHC-I molecules in our transfected cells. The effects of Dynasore, a small molecule that inhibits the activity of dynamin, on patch dynamics was determined and it was found to be an effective tool for manipulating (reducing) vesicle arrival rate. Quantification of vesicle arrival rates allowed for a direct measurement of the effects of Dynasore, clearly showing that the arrival rate of MHC-I decreases as the concentration of Dynasore increases. Dynasore is a drug that inhibits the clathrin-coated vesicle mechanism, thus is implicated in hindering endocytosis. However, results from a number of laboratories implicate dynamin in exocytic events (Jaiswal et al., 2009; Anantharam et al., 2011, 2012). Hence, Dynasore-mediated modulation of vesicle traffic might be both indirect, through its effects on endocytosis, and direct, through its effects on exocytosis. Regardless of the mechanism involved, our model assumed equal exocytosis and endocytosis rates, to ensure a constant cell surface, and this phenomenon is supported by the fact that no increase in the cell surface is observed over the timecourse of our measurements, and that fluorescence intensity does not continuously increase (which would be the case if MHC-I is delivered at higher rates than it is internalized). We chose to count only exocytosis events because of technical considerations: detection of a sharp local increase in fluorescence intensity is much more reliable than a local decrease, which might easily drop into the experimental noise of the system. We postulate, however (based on the arguments presented above) that endocytosis occurs at the same rates as exocytosis.

Measuring apparent patch sizes following treatment with different Dynasore concentrations showed that the mean patch size increases with Dynasore concentration, in agreement with previously reported data using other methods to slow vesicle traffic (Tang and Edidin, 2001). Here, a spatial (2D) autocorrelation procedure was used to measure the average size of patches in a cropped image. Each single cell image was cropped into several smaller images (crops), in order to exclude background (which tremendously influences the results of autocorrelation). Consequently, the graphs in Fig. 2A–D depict a distribution of patch sizes obtained from hundreds of different crops made from tens of cell images, averaging thousands of patches for each treatment. The ability to average such numbers of patches makes the autocorrelation approach much more reliable and bias-free compared to manually measuring individual patches. The resulting patch size distributions show heterogeneity of patch sizes, similar for all treatments. The comparison between the means of these distributions shows a statistical difference between them, when cells are treated with different Dynasore concentrations.

Our model predicts that there is a relationship between MHC-I arrival rate and patch size. Although this was discussed previously (Tang and Edidin, 2003), the effect was demonstrated using either

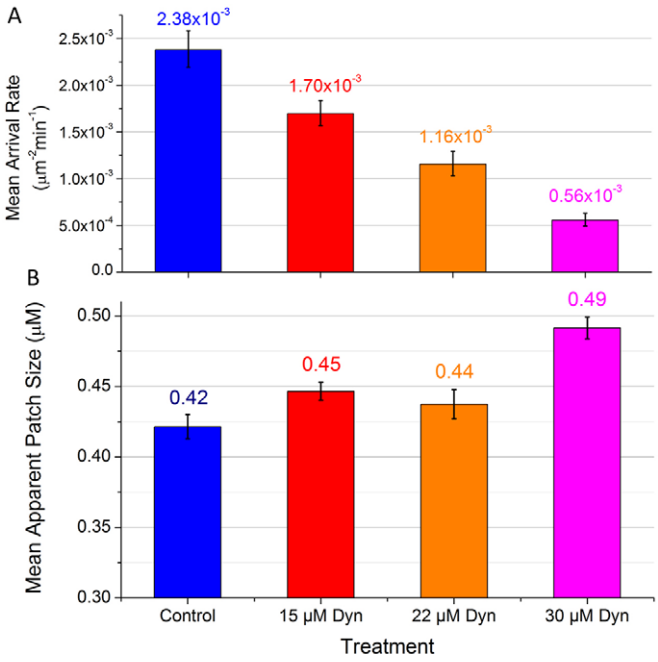

Fig. 5. Vesicle arrival rate directly determines apparent size of MHC-I patches. As arrival rate of MHC-I to the membrane decreases (A), the patch size increases (B). This measurement is consistent with the prediction of our simulation-based model and constitutes its experimental validation. Results are mean±s.e.m. *n* values are as given in Figs 1 and 2 for graphs in A and B, respectively.

Journal of Cell Science (2016) 129, 3342-3350 doi:10.1242/jcs.187112

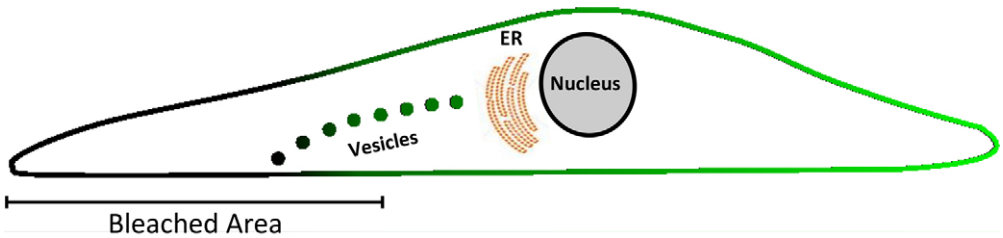

Fig. 6. Schematic representation of Gaussian bleaching effects on the cell. Green and black regions correspond to fluorescing and bleached areas, respectively, of the membrane. Given that bleaching is Gaussian, some areas are partially bleached, represented by dark green. The train of dots, changing from black to green, represents vesicles carrying GFP–MHC-I, with increasing fluorescence intensity.

hypertonic medium treatment or dynamin mutant cells, and in both cases cells were fixed and immunostained for MHC-I. Given that in fixed cells, one cannot quantify the arrival rate, these results can only be considered indirect supporting evidence for our model prediction. Here, we imaged live cells that express GFP-tagged MHC-I molecules using real-time TIRFM, allowing a direct measurement of both arrival rate and patch size on the same sample. Furthermore, replacing the hypertonic medium treatment or dynamin mutant with Dynasore treatment permits a dose–response measurement of the effect of arrival rate reduction on patch size. These changes in the experimental design allow us to show for the first time, the (inverse) correlation between these parameters (Fig. 5). The persistence of MHC-I patches at steady state was predicted to be a result of a combination of vesicle trafficking and escape over transient barriers to free diffusion (Gheber and Edidin, 1999). In the absence of an active mechanism that replenishes the local concentration, as MHC-I molecules diffuse away from the patches they disperse towards a uniform distribution on the membrane (Fig. S2). These results corroborate the prediction of our model and are the last step in the validation of our model. Along with our previous results (Lavi et al., 2007, 2013), we present a complete, comprehensive view on the spatio-temporal dynamics of MHC-I patches.

Our model assumes that sites of vesicle fusion are randomly distributed across the cell surface. Though this constitutes a worst-case scenario, given that it is the least favorable for maintaining patches at a steady state, simulations showed that patches form and persist even under these conditions. It is clear, however, that a non-random distribution of delivery sites will be a more favorable scenario for MHC-I patch formation. We used FRAP in order to compare patch distributions in the same large membrane area at two different time points, imaging patches, then 'erasing' the fluorescence by prolonged bleaching and then allowing patches to reform. We found that that ~80% of MHC-I patches recover to the same location that patches were seen before bleaching. This means that vesicle traffic is targeted to specific locations on the membrane.

The data from our experiments contains information on diffusion of the MHC-I molecules. Though the experiment violates a number of the boundary conditions for conventional FRAP, we were able to use our recently developed simulation approach 'simFRAP' (Blumenthal et al., 2015) to extract diffusion coefficients. (The simFRAP algorithm is freely available as an ImageJ plugin at: http://imagej.nih.gov/ij/plugins/sim-frap/index.html). We found that recovery of patches after bleaching has two temporally separated components, diffusion in the early stages of recovery followed by an increase in intensity that is larger than expected from pure diffusion. We propose that the latter is a result of new fluorescent MHC-I molecules delivered to the cell surface.

The delay in this component of recovery, which is detectable at ~9 min after bleaching, is due to the fact that the laser beam bleaches the whole depth of a cell. Therefore, besides surface molecules, trafficking vesicles loaded with fluorescent MHC-I molecules are bleached. Hence, new molecules arriving at the cell surface immediately after bleaching are not fluorescent and so do not contribute to the recovery of fluorescence measured by our probe beam. On the other hand, GFP–MHC-I molecules synthesized after photobleaching, or in areas not reached by the bleaching beam, once introduced into the delivery pathway make their way towards the plasma membrane. Therefore, the vesicles arriving to the membrane following the photobleaching event form a train of increasingly fluorescent vesicles (Fig. 6). This mechanism is also supported by the fact that we do not observe 'blinking' (sudden appearance) of patches after photobleaching, but instead a gradual increase in their intensity, as they form anew.

The observed recovery curve is therefore a sum of two increasing intensity profiles: one represents recovery by lateral diffusion from the unbleached portion of the cell and the second represents the gradual increase in fluorescence of delivered vesicles. The 'knee' at ~9 min is the cross-over point from the predominant (fast) recovery by diffusion that is almost saturating (Fig. 7, red line), to the (slower) increase in fluorescence due to delivery of vesicles (Fig. 7, green line). The time for synthesis of H2-L^{d} exogenously expressed in L-cells and its traffic to the trans-Golgi network is in the order of tens of minutes (Zuniga and Hood, 1986). Analysis of the bleached

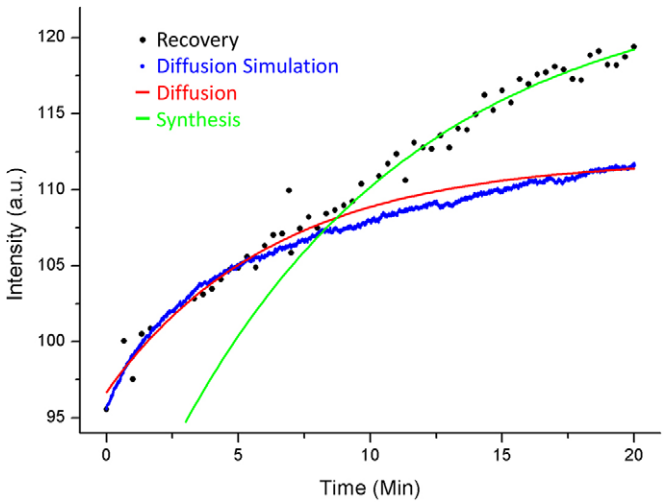

Fig. 7. The fluorescence recovery curve is a sum of two increasing intensity profiles. Recovery is a sum of two components: recovery by lateral diffusion from the unbleached portion of the cell (red line) and increase in fluorescence due to delivery of vesicles (green line). The simulation (blue dots) compares nicely to the diffusion recovery component, and yields a well-established lateral diffusion coefficient of $9.18\pm0.15\times10^{-8}$ cm^2/s (mean±s.d.).

Journal of Cell Science (2016) 129, 3342-3350 doi:10.1242/jcs.187112

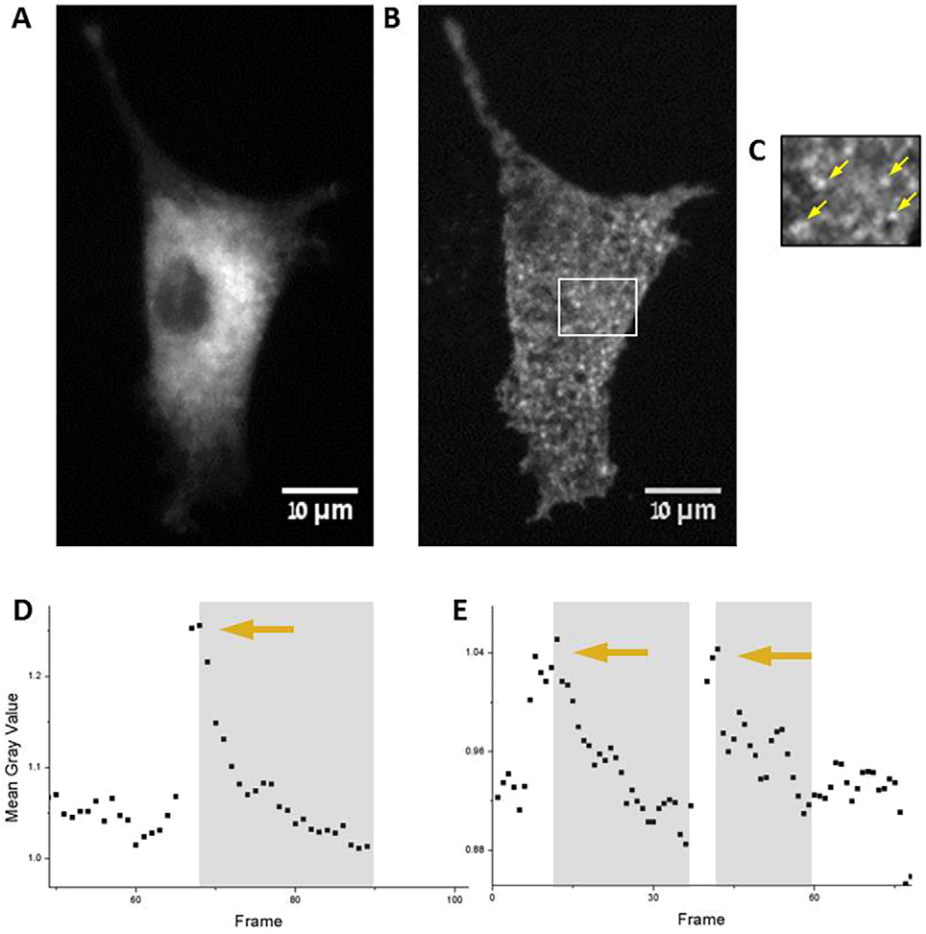

Fig. 8. A cell expressing GFP-tagged MHC-I imaged in two different modes. Both images are taken at the same focal distance. (A) Conventional epi-fluorescence image where the dark nucleus is visible surrounded by a bright region corresponding to the endoplasmic reticulum and Golgi. (B) TIRFM image where the MHC-I patches on the plasma membrane are clearly observed as bright dots, and no fluorescence from the cell volume is excited. (C) Magnification of the indicated area in B showing (diffraction limited) fluorescent patches (some examples are marked by yellow arrows). (D,E) Examples of arrival events. Plots of intensity as a function of time (frames in a time-lapse series) of single patches; each plot refers to a single region on the membrane – i.e. a single patch. Peaks in intensity (marked by arrows) suggest arrival of new molecules to the membrane, vesicle arrival events; a fusion event will be followed by an exponential decay in intensity (gray box in the figure). (D) Single arrival event. (E) Two consecutive arrival events at the same location.

area recovery suggests that the time scale for trafficking matured (endoH-resistant) MHC-I molecules to the plasma membrane is ~10 min.

Overall, our results estimate the time for trafficking newly synthesized MHC-I molecules to the surface, the requirement for this trafficking to maintain patches of MHC-I molecules at the cell surfaces, and the selectivity, non-randomness, of sites for exocytosis. MHC-I molecules are typical type-I membrane proteins, and we suggest that our results for this molecule can be generalized for other transmembrane proteins, accounting for their distribution on the cell surface.

MATERIALS AND METHODS

Cell culture

All reagents were purchased from Biological Industries (Kibbutz Beit Haemek, Israel) unless otherwise noted. Normal mouse fibroblasts [L-M(tk), ATCC CCL-1.3] expressing MHC-I, H-2L^d tagged with GFP (Marguet et al., 1999), were cultured in 250-ml tissue culture flasks (Cellstar, GrenierBio-One, Frickenhausen, Germany) at 37°C and 5% CO_2 in Roswell Park Memorial Institute medium (RPMI-1640) without L-glutamine, with 10% fetal bovine serum and 0.22 mg/ml G418 (geneticin; Sigma, St Louis, MO). Cells were screened for contamination of mycoplasma. For microscopy, flasks were washed with 10 ml of phosphate-buffered saline (PBS), then cells were detached from flasks by incubating in 2 ml trypsin EDTA 0.25% for 2 min at 37°C and centrifuging for 5 min at 280 ***g***. Cells, in 5 ml medium, were then transferred to plastic petri dishes with glass coverslip inserts. After overnight incubation, medium was removed and dishes were gently rinsed three times with 5 ml of warmed (37°C) Hepes-buffered Hank's balanced salt solution. Cells treated with Dynasore (Sigma) were later incubated with warmed (37°C) 15 µM, 22 µM or 30 µM Dynasore solution for 30 min and then imaged for a maximum time of 45 min.

Imaging

TIRFM

We used a homemade prism-based TIRFM system to image vesicle traffic. The system uses an argon ion laser (35 MAP 321, Melles Griot laser group, Carlsbad, CA) at 488 nm as the excitation light source. Cells were imaged with a SPOT charge-coupled device camera (Diagnostic Instruments, Sterling Heights, MI), mounted on a Zeiss (Oberkochen, Germany) Axioplan2 upright fluorescence microscope with a 40×0.8 N.A. water objective.

Total internal reflection illumination creates an evanescent field at the interface between glass and the cell membrane. The field decays exponentially into the cell with a penetration depth of ~100 nm (Axelrod, 2008), thus exciting fluorescence primarily in the cell plasma membrane. In our instrument, fluorescence is excited in the lower membrane adhered to the glass, and emitted light is collected by an upright microscope. Fig. 8 compares the images obtained on the same cell in epi-fluorescence (Fig. 8A) and TIRFM (Fig. 8B). MHC-I patches are clearly visible in Fig. 8C, owing to the exclusion of fluorescence from within the cell volume. Both images are taken at the same focal plane. However, the exposure in Fig. 8A is much shorter, due to the bright fluorescence from the whole cell volume, which causes the cell edges to appear fuzzier.

FRAP

Photobleaching was performed using a 100 mW solid-state laser (Laserglow technologies, Toronto, Ontario, Canada) emitting at 473 nm. The laser beam was attenuated by a neutral density filter (T=30%) to avoid damage to the cells, and entered the upright microscope through the epi-illumination port and was concentrated through the objective onto the sample. Laser burst

time was controlled by a Transistor–Transistor Logic (TTL) 5 V signal created by a function generator (Tabor Electronics, Tel Hanan, Israel) set to a 1 Hz square wave.

Alignment using cross-correlation

In order to align an image series, we have calculated the 2D spatial cross correlation between consecutive frames. First, the (x,y) displacement of its maximum with respect to the origin (0,0) was determined. This displacement represents the spatial shift between the two images, therefore the second image was shifted by the (x,y) displacement values, thus aligning it to the first one. The procedure was repeated for the next pair of frames, until reaching the end of the stack. In the bleaching experiments, the same approach was implemented, using the unbleached part of the cell only. Then, these values are used to properly align the pre-bleach and post-bleach frames.

Arrival rate analysis

A sequence of images was taken; exposure time, frame number and total time of sampling were recorded. Individual cropped series were created for each cell and inputted into the image sequence time derivative algorithm (see below). The algorithm result was scanned frame by frame for suspected arrival events (SAEs). Given that fluorescence intensity reports the relative number of molecules, a peaking of intensity describes a vesicle arrival event, delivering new MHC-I molecules to the cell surface. In order to determine if a SAE is an arrival event, intensity versus time profiles were extracted from the SAE position. Following photobleaching and background correction, the time profile of each SAE was inspected against an arrival pattern (Lavi et al., 2007), a peak in intensity, suggesting an arrival event, followed by an exponential decay, characteristic of the obstructed diffusion of molecules outside the patch, with a previously reported characteristic decay time ('patch lifetime') of ∼40 s (Lavi et al., 2007) (see examples in Fig. 8D,E). Only arrival events verified according to this procedure were counted, and included in the calculation of arrival rate (arrivals/μm^2 min).

Image sequence time derivative algorithm

A custom IDL algorithm (Interactive Data Language, Exelis, Boulder, CO, USA) was employed to produce a time derivative stack from an acquired stack of consecutive frames. The algorithm receives a stack (Fig. S3A) as input and implements three procedures on it: (1) alignment of all stack frames to the first one using a cross-correlation procedure; (2) reduction of peaking noise by implementation of a median filter on trios of frames; and (3) production of a new stack in which each frame is the difference of two consecutive frames (Fig. S3B).

Implementing a time derivative procedure on a stack of frames eliminates unchanged fluorescent areas from each frame, therefore removing static background. The newly created stack shows only the differences between two original consecutive frames, allowing the detection of low-signal arrival events (Fig. S3C). The algorithm can be obtained from the authors upon request.

Patch size algorithm

A custom IDL algorithm was employed to quickly extract the mean patch size from an image (Fig. S4A), using a procedure similar to in Hwang et al. (1998). The input frame is first cropped to several small images, in order to exclude background. Then, each individual crop is (2D) space-autocorrelated (Fig. S4B), and the result is radially averaged around the center of the frame (Fig. S4C). The intensity profile along the diameter of the averaged frame (Fig. S4C, red line) is extracted and fitted to a Gaussian curve (Fig. S4D, Gaussian curve in red). The full width at half maximum (FWHM) of the fitted Gaussian curve is representative of the typical object size in the original crop (patch size) and is extracted in pixels. In order to receive the actual typical size, the algorithm uses a built-in calibration curve to translate the extracted FWHM (in pixels) to the actual typical object size (in μm). The (linear) calibration curve (Fig. S4E) was achieved by running the algorithm on synthetic images created with different known object sizes.

Hindering MHC-I vesicle trafficking to the membrane increases the apparent patch size

MHC-I molecules diffuse away from the patches by escaping past barriers to free diffusion. In the absence of an active mechanism that replenishes the local concentration of molecules in the patch (i.e. vesicle traffic), patches disperse towards a uniform distribution on the membrane. Comparison between synthetic spatial intensity profiles of typical patches from the four different groups (Fig. S2) shows the changes in patch profile once vesicle trafficking is reduced (as a result of Dynasore treatment). The synthetic intensity profiles are shown as Gaussian curves, approximating circular MHC-I patches on the membrane. As patches disperse, the same amount of MHC-I molecules is spread over a larger area, by diffusion. The Gaussian curves all cover the same area; however, their peak intensity decreases and their FWHM increases with increased Dynasore concentration.

Competing interests

The authors declare no competing or financial interests.

Author contributions

D.B. performed the experiments, wrote the algorithms, analyzed the data, interpreted the experiments and wrote the manuscript. M.E. provided the fibroblast cells, provided experimental advice and support, and contributed to writing the manuscript. L.A.G. provided experimental advice, wrote the manuscript and provided funding support.

Funding

The authors gratefully acknowledge a grant from the United States-Israel Binational Science Foundation [grant number 2009345]; this work was also partially supported by the Focal Technological Area program of the Israeli National Nanotechnology Initiative (INNI).

Supplementary information

Supplementary information available online at
http://jcs.biologists.org/lookup/doi/10.1242/jcs.187112.supplemental

References

Anantharam, A., Bittner, M. A., Aikman, R. L., Stuenkel, E. L., Schmid, S. L., Axelrod, D. and Holz, R. W. (2011). A new role for the dynamin GTPase in the regulation of fusion pore expansion. *Mol. Biol. Cell* **22**, 1907-1918.

Anantharam, A., Axelrod, D. and Holz, R. W. (2012). Real-time imaging of plasma membrane deformations reveals pre-fusion membrane curvature changes and a role for dynamin in the regulation of fusion pore expansion. *J. Neurochem.* **122**, 661-671.

Axelrod, D. (2008). Total internal reflection fluorescence microscopy. *Method Cell Biol.* **89**, 169-221.

Blumenthal, D., Goldstien, L., Edidin, M. and Gheber, L. A. (2015). Universal approach to FRAP analysis of arbitrary bleaching patterns. *Sci. Rep.* **5**.

Edidin, M. (1987). Rotational and lateral diffusion of membrane proteins and lipids: phenomena and function. **29**, 91-127.

Edidin, M., Zuniga, M. C. and Sheetz, M. P. (1994). Truncation mutants define and locate cytoplasmic barriers to lateral mobility of membrane glycoproteins. *Proc. Natl. Acad. Sci. USA* **91**, 3378-3382.

Engelman, D. M. (2005). Membranes are more mosaic than fluid. *Nature* **438**, 578-580.

Feder, T. J., Brust-Mascher, I., Slattery, J. P., Baird, B. and Webb, W. W. (1996). Constrained diffusion or immobile fraction on cell surfaces: a new interpretation. *Biophys. J.* **70**, 2767-2773.

Fooksman, D. R., Gronvall, G. K., Tang, Q. and Edidin, M. (2006). Clustering class I MHC modulates sensitivity of T cell recognition. *J. Immunol.* **176**, 6673-6680.

Gheber, L. A. and Edidin, M. (1999). A model for membrane patchiness: lateral diffusion in the presence of barriers and vesicle traffic. *Biophys. J.* **77**, 3163-3175.

Gowrishankar, K., Ghosh, S., Saha, S., C, R., Mayor, S. and Rao, M. (2012). Active remodeling of cortical actin regulates spatiotemporal organization of cell surface molecules. *Cell* **149**, 1353-1367.

Haucke, V., Neher, E. and Sigrist, S. J. (2011). Protein scaffolds in the coupling of synaptic exocytosis and endocytosis. *Nat. Rev. Neurosci.* **12**, 127-138.

Houy, S., Croisé, P., Gubar, O., Chasserot-Golaz, S., Tryoen-Tóth, P., Bailly, Y., Ory, S., Bader, M. F. and Gasman, S. Exocytosis and Endocytosis in Neuroendocrine Cells: Inseparable Membranes! *Front. Endocrinol.* **4**, 135.

Hwang, J., Gheber, L. A., Margolis, L. and Edidin, M. (1998). Domains in cell plasma membranes investigated by near-field scanning optical microscopy. *Biophys. J.* **74**, 2184-2190.

Jaiswal, J. K., Rivera, V. M. and Simon, S. M. (2009). Exocytosis of post-golgi vesicles is regulated by components of the endocytic machinery. *Cell* **137**, 1308-1319.

Kusumi, A. and Sako, Y. (1996). Cell surface organization by the membrane skeleton. *Curr. Opin. Cell Biol.* **8**, 566-574.

Lavi, Y., Edidin, M. A. and Gheber, L. A. (2007). Dynamic patches of membrane proteins. *Biophys. J.* **93**, L35-L37.

Lavi, Y., Gov, N., Edidin, M. and Gheber, L. A. (2012). Lifetime of major histocompatibility complex class-I membrane clusters is controlled by the actin cytoskeleton. *Biophys. J.* **102**, 1543-1550.

Lavi, Y., Edidin, M. and Gheber, L. A. (2013). Lifetime of major histocompatability complex class I membrane clusters is controlled by the actin cytoskeleton. *Biophys. J.* **104**, 392a.

Macia, E., Ehrlich, M., Massol, R., Boucrot, E., Brunner, C. and Kirchhausen, T. (2006). Dynasore, a cell-permeable inhibitor of dynamin. *Dev. Cell* **10**, 839-850.

Marguet, D., Spiliotis, E. T., Pentcheva, T., Lebowitz, M., Schneck, J. and Edidin, M. (1999). Lateral diffusion of GFP-tagged H2L(d) molecules and of GFP-TAP1 reports on the assembly and retention of these molecules in the endoplasmic reticulum. *Immunity* **11**, 231-240.

Patzak, A. and Winkler, H. (1986). Exocytotic exposure and recycling of membrane antigens of chromaffin granules: ultrastructural evaluation after immunolabeling. *J. Cell Biol.* **102**, 510-515.

Robinson, I. M., Finnegan, J. M., Monck, J. R., Wightman, R. M. and Fernandez, J. M. (1995). Colocalization of calcium entry and exocytotic release sites in adrenal chromaffin cells. *Proc. Natl. Acad. Sci. USA* **92**, 2474-2478.

Sako, Y. and Kusumi, A. (1995). Barriers for lateral diffusion of transferrin receptor in the plasma membrane as characterized by receptor dragging by laser tweezers: fence versus tether. *J. Cell Biol.* **129**, 1559-1574.

Smith, C. and Neher, E. (1997). Multiple forms of endocytosis in bovine adrenal chromaffin cells. *J. Cell Biol.* **139**, 885-894.

Tang, Q. and Edidin, M. (2001). Vesicle trafficking and cell surface membrane patchiness. *Biophys. J.* **81**, 196-203.

Tang, Q. and Edidin, M. (2003). Changes in the patchiness of a membrane protein after inhibiting vesicle traffic imaged by total internal reflection fluorescence microscopy. *Biophys. J.* **84**, 211a.

Turley, S. J., Inaba, K., Garrett, W. S., Ebersold, M., Unternaehrer, J., Steinman, R. M. and Mellman, I. (2000). Transport of peptide-MHC class II complexes in developing dendritic cells. *Science* **288**, 522-527.

Vereb, G., Szollosi, J., Matko, J., Nagy, P., Farkas, T., Vigh, L., Matyus, L., Waldmann, T. A. and Damjanovich, S. (2003). Dynamic, yet structured: the cell membrane three decades after the Singer-Nicolson model. *Proc. Natl. Acad. Sci. USA* **100**, 8053-8058.

Yamada, H., Abe, T., Li, S.-A., Masuoka, Y., Isoda, M., Watanabe, M., Nasu, Y., Kumon, H., Asai, A. and Takei, K. (2009). Dynasore, a dynamin inhibitor, suppresses lamellipodia formation and cancer cell invasion by destabilizing actin filaments. *Biochem. Biophys. Res. Commun.* **390**, 1142-1148.

Yechiel, E. and Edidin, M. (1987). Micrometer-scale domains in fibroblast plasma membranes. *J. Cell Biol.* **105**, 755-760.

Zuniga, M. C. and Hood, L. E. (1986). Clonal variation in cell surface display of an H-2 protein lacking a cytoplasmic tail. *J. Cell Biol.* **102**, 1-10.

Journal of Cell Science